

Intersite Coulomb Interactions in Charge Ordered Systems

Bo Gyu Jang,^{1,*} Minjae Kim,^{1,†} Sang-Hoon Lee,¹ Wooil Yang,^{2,1} Seung-Hoon Jhi,² and Young-Woo Son^{1,‡}

¹Korea Institute for Advanced Study, Seoul 02455, Republic of Korea

²Department of Physics, Pohang University of Science and Technology, Pohang 37673, Republic of Korea

(Dated: March 27, 2023)

Using *ab initio* approaches for extended Hubbard interactions coupled to phonons, we reveal that the intersite Coulomb interaction plays important roles in determining various distinctive phases of the paradigmatic charge ordered materials of $\text{Ba}_{1-x}\text{K}_x\text{AO}_3$ ($A = \text{Bi}$ and Sb). We demonstrated that all their salient doping dependent experiment features such as breathing instabilities, anomalous phonon dispersions, and transition between charge-density wave and superconducting states can be accounted very well if self-consistently obtained nearest neighbor Hubbard interaction are included, thus establishing a minimal criterion for reliable descriptions of spontaneous charge orders in solids.

Since Verwey found the metal-to-insulator transition (MIT) in magnetite (Fe_3O_4) owing to long-range order of alternating Fe^{2+} and Fe^{3+} ions [1], the charge ordered state has been one of the central issues in condensed matter physics. It often occurs near MITs, superconducting (SC), or charge density wave (CDW) states [2–9]. These local charge ordering (CO) can lead to colossal magnetoresistance, ferroelectricity or multiferroicity [10, 11]. In addition, the CO in high-temperature cuprate superconductors has also been studied intensively to understand its roles as a leading competitor of SC state [4–7].

Charge ordered materials host atoms with disparate charging states that are closely placed, invoking the strong Coulomb interactions and distorting lattices to relieve their energetic cost [12]. Hence, theories for the systems should treat the interaction as well as its coupling to lattices on an equal footing. Typical approaches based on density functional theory with the local density approximation (DFT-LDA) [13] or generalized gradient approximation (GGA) [14] fail to describe their properties [15, 16]. The addition of on-site Hubbard interaction (U) within DFT (DFT+ U) [17, 18] captures a correct CO state when the intersite interaction is screened [15]. Except few cases, however, it is insufficient in obtaining the ground states [19–21]. Therefore, advanced methods beyond the local corrections are needed to figure the role of the interactions in COs.

Perovskite BaBiO_3 (BBO) and BaSbO_3 (BSO) are prototypical CO materials that are not well understood by DFT-GGA and DFT+ U [22–34]. They show CDW states characterized by breathing distortion of oxygen octahedra with the charge disproportionations of Bi ions [22–24]. The CDW is suppressed by substituting Ba with K and SC phase occurs at a relatively higher transition temperature (T_c) [8, 9]. A few recent studies based on the Heyd-Scuseria-Ernzerhof (HSE) hybrid functional and GW approximation (GWA) can capture the insulating ground state of BBO and obtain enhanced electron-phonon (e - ph) interactions, providing a clue to understanding the observed T_c [31–35]. However, realistic full phonon spectra to understand the transition between SC and CDW states for experimentally accessible doping lev-

els are hardly available due to demanding computational resources and computed frequency is usually overestimated for strongly coupled phonons [26, 33, 34].

On the other hand, recent developments on self-consistent evaluations of U [36, 37] and intersite Hubbard interactions (V) [38, 39] within DFT (DFT+ U + V) [40] successfully describe various properties of solids [38–49]. Owing to their low computational cost comparable to DFT-LDA and improved accuracy to GWA [38, 46], the new method provides an opportunity to study the correlated solids in large scale structures and full phase space of interests. Motivated by these developments as well as the works on BBO and BSO, we have carried out *ab initio* study to explore the role of the interactions for interplay between their electronic and structural properties.

In this Letter, we theoretically demonstrate that the evolution of charge ordered states in bismuthates and antimonates with potassium doping is essentially controlled by the doping-dependent non-local Coulomb interaction. Our new parameter-free *ab initio* method for extended Hubbard interactions [38, 46] can compute electronic energy bands as well as full phonon dispersions of $\text{Ba}_{1-x}\text{K}_x\text{AO}_3$ ($A = \text{Bi}$ and Sb) for the whole phase space with structural phase transitions, agreeing well with all the key measurements only when intersite Coulomb interactions are included. Our establishments imply that the explicit treatment of the non-local interactions is critical for the description of the intertwined charge and lattice degrees of freedom in charge ordered materials.

Our DFT+ U + V method uses the total energy functional of $E_{\text{tot}} = E_{\text{DFT}} + E_{\text{Hub}}$ that can be decomposed into (semi)local density functional of E_{DFT} and Hubbard functional with double counting corrections [40], $E_{\text{Hub}} = \frac{1}{2} \sum_I U_I \sum_{m,m',\sigma} (\delta_{mm'} - n_{mm'}^{II\sigma}) n_{m'm}^{II\sigma} - \frac{1}{2} \sum_{\{I,J\}} V_{IJ} \sum_{m,m',\sigma} n_{mm'}^{IJ\sigma} n_{m'm}^{JI\sigma}$, where the generalized occupation matrix is $n_{mm'}^{IJ\sigma} = \sum_{\mathbf{k}\nu} f_{\mathbf{k}\nu}^\sigma \langle \psi_{\mathbf{k}\nu}^\sigma | \phi_m^I \rangle \langle \phi_{m'}^J | \psi_{\mathbf{k}\nu}^\sigma \rangle$, $f_{\mathbf{k}\nu}^\sigma$ the Fermi-Dirac function of Kohn-Sham orbital of $\psi_{\mathbf{k}\nu}^\sigma$ of the ν th band with spin σ at momentum \mathbf{k} , and ϕ_m^I the localized orbitals with angular quantum number m . Here, I and J are abbreviated indexes for atomic positions and principal and azimuthal quan-

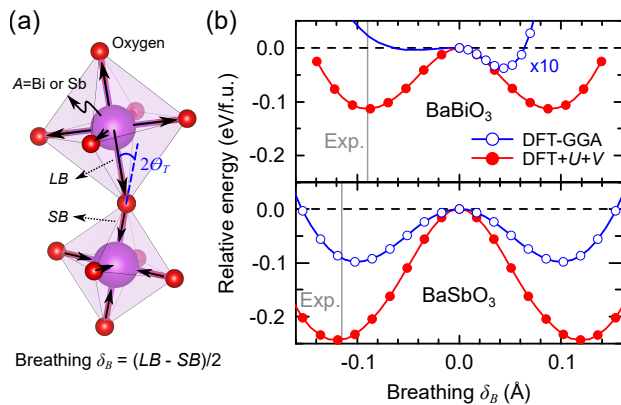


FIG. 1. (a) Atomic model for distorted octahedra in CDW state of BB(S)O. Breathing distortion of δ_B and tilting angle of θ_T are defined as an averaged length difference between Bi(Sb)-O bonds and as an angle between vertical axes belong to adjacent octahedra, respectively. (b) Double well potential as a function of δ_B . Blue, red, and grey lines indicate DFT-GGA, DFT+ $U+V$ and experiments [24, 51], respectively. The DFT-GGA results for $\delta_B > 0$ are enlarged by ten times to show the minimum for breathing distortion clearly.

tum numbers together and $\{I, J\}$ denotes a pair of atoms within the nearest neighboring distances. We obtain self-consistent U_I and V_{IJ} using new pseudohybrid functionals for Hubbard interactions [36–39]. We also consider rotationally invariant interactions [38, 40] so that U and V for valence s and p orbitals of Bi (Sb) and $2p$ orbital of O are computed as shown in Table I. Detailed parameters are in Supplementary Materials (SM) [50].

At low-temperature, BBO is the monoclinic structure having oxygen octahedra with breathing distortion of displacement by δ_B and a tilting angle of θ_T between them as shown in Fig. 1(a), while BSO has δ_B only, resulting in fcc structure (Fm $\bar{3}$ m) [24]. We first investigate the artificial double-well potential induced by δ_B without tilting [Fig.1(b)]. For BBO, our DFT-GGA calculation underestimates δ_B with a very shallow potential well [26, 28]. The breathing distortion, however, is significantly enhanced in DFT+ $U+V$ calculation. Unlike BBO, BSO has a relatively deep potential with DFT-GGA. Nonetheless, the energy gain from the breathing distortion in BSO also becomes larger with the extended Hubbard interactions.

TABLE I. Calculated U and V (in eV) for BaAO_3 ($A = \text{Bi}$ and Sb). $U_{s(p)}^A$ (U_p^O) is on-site Hubbard parameters of valence $s(p)$ orbital of $A(O)$ atom. $V_{sp(pp)}$ is the intersite Hubbard parameters between $s(p)$ orbital of A and p orbital of O.

A	U_s^A	U_p^A	U_p^O	V_{sp}	V_{pp}
Bi	1.03	0.11	8.18	1.78	1.59
Sb	0.92	0.13	8.18	1.86	1.61

As shown in the model potential wells in Fig. 1 (b), DFT+ $U+V$ well captures a part of CDW states of the undoped cases. Our results on a fully relaxed monoclinic BBO are summarized and compared with the previous studies (Table II). If tilting of θ_T is allowed, DFT-GGA accidentally reproduces δ_B owing to its overestimation of volume by $\sim 4\%$ and θ_T by $\sim 14\%$ but still cannot describe the insulating gap of CDW state like a previous work [31]. On the other hand, DFT+ $U+V$ calculation well describes all the critical experimental parameters.

To investigate the effects of U and V in metallic BBO above the CDW transition temperature of 800 K, we compute the energy bands of BBO in the perfect cubic perovskite phase with experimental volume, using DFT-GGA, DFT+ $U+V$, and GWA as shown in Figs. 2 (a) and (b). The width of the energy band crossing the Fermi level (E_F) is enhanced with both DFT+ $U+V$ and GWA compared with one with DFT-GGA. We also note that the DFT-GGA bands for fully occupied states associated with oxygen p orbitals shifted down by including U_p^O in the DFT+ $U+V$ and by the self-energy corrections in the GWA method.

Effects of intersite interaction are also conspicuous for electronic structures of the CDW state. Figure 2 (c) shows the calculated density of states (DOS) of BBO with the fully relaxed monoclinic CDW structure obtained from each method (Table II) together with previous GWA results and photoemission spectroscopy (PES) data [53, 54]. The two experiments show the quite different positions of the highest PES peak below E_F (-3 eV and -5 eV, respectively), that may originate from the different substrate conditions [54]. As shown in Fig. 2(c), the DOS peak position for oxygen $2p$ orbitals from DFT-GGA is significantly off the experimental one. Furthermore, the energy gap of CDW state is absent despite the correct δ_B . Unlike DFT-GGA results, the DOS using DFT+ $U+V$ well agrees with the experiments and the previous GWA calculation [31]. The O $2p$ peak position is located at around -4 eV, which is in between two experimental results. The band gap is about 1 eV, consistent with the experimental results. Although U_p^O

TABLE II. Calculated structural and electronic properties of BBO along with computational and experimental data from previous studies. v : volume, β : monoclinic angle, δ_B : breathing distortion, θ_T : tilting distortion, and E_g : band gap

	Experiments ^a	HSE ^b	DFT-GGA	DFT+ $U+V$
v (\AA^3)	81.80 \sim 82.54	82.10	85.03	82.94
β (deg)	90.16 \sim 90.27	90.24	90.39	90.34
δ_B (\AA)	0.08 \sim 0.09	0.09	0.08	0.10
θ_T ($^\circ$)	10.12 \sim 10.72	11.9	11.75	10.46
E_g (eV)	0.8 \sim 1.1	0.84	0.0	0.99

^a References 22, 51, and 52

^b Reference 31

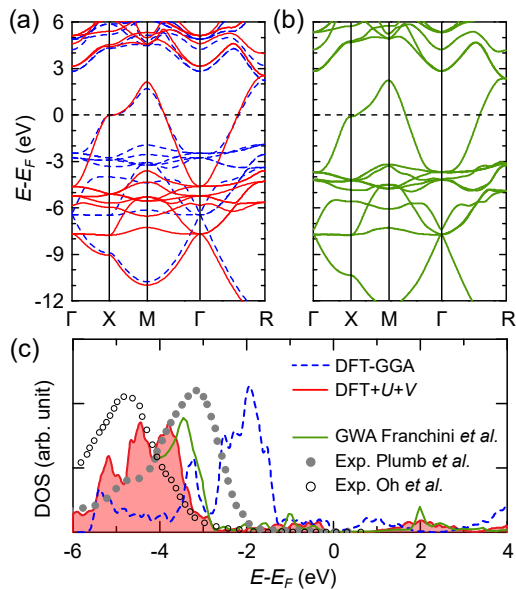


FIG. 2. Energy bands of BBO of cubic perovskite structure obtained from (a) DFT (blue) and DFT+ $U+V$ (red) and (b) GWA method. Here we use GW_0 approximation for the GWA. (c) Density of states for monoclinic CDW structure. Blue, red, and green line indicate DFT, DFT+ $U+V$ and previous GWA results [31], respectively. Empty circles are from photoemission spectroscopy measurements [53, 54].

is critical for the down shifted bands for O $2p$ orbitals, we note that the DFT+ U without V still substantially underestimates the CDW band gap (Table S1 in the SM).

The results so far demonstrate that our new method describes correctly the electronic and structural properties of undoped bismuthate and antimonates without serious computational costs. Thus, it enables the study of the non-local interaction effects on phonons with various K doping levels thoroughly, which could not be done with HSE or GWA method easily. From now on, we present the comprehensive phonon dispersions using the frozen phonon techniques [55] with extended Hubbard interactions to examine the structural instability of potassium doped $Ba_{1-x}K_xBiO_3$ and $Ba_{1-x}K_xSbO_3$ (BKBO and BKSO). Related computational details are in SM [50].

Figure 3 (a) shows the phonon dispersion and DOS of $Ba_{0.6}K_{0.4}BiO_3$ together with experimental data [56, 57]. Here we focus four representative phonon modes related with CDW states in BKBO and BKSO systems; stretching and in-phase tilting modes at M point and breathing and anti-phase tilting modes at R point. For stretching mode, Bi-O bond length changes along only two axes of oxygen octahedron while it changes along all three axes in the breathing mode. In Fig. 3(a), it is immediately noticeable that the unstable in(anti)-phase tilting mode at $M(R)$ point obtained by DFT-GGA hardens enough to be stable when V is included, agreeing with experiments. Not only low frequency modes, but the high frequency

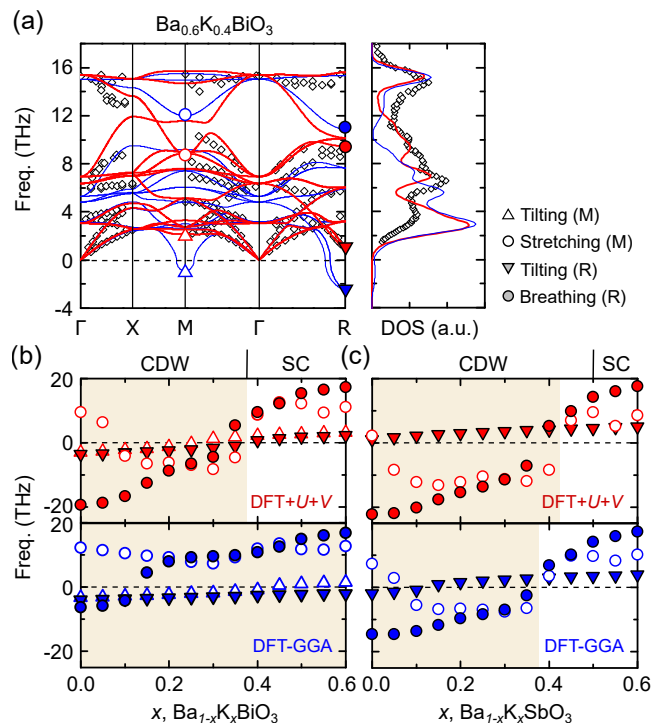


FIG. 3. (a) Phonon dispersion and DOS of $Ba_{0.6}K_{0.4}BiO_3$. Open diamonds and blue (red) lines indicate experiments [56, 57] and the DFT-GGA (DFT+ $U+V$) results, respectively. Frequencies of the four selected modes are marked by open and filled triangles and circles at M and R points, respectively. Phonon frequency variations of the four modes as increasing K doping level in (b) BKBO and (c) BKSO. Top and bottom panels are for the modes obtained by DFT+ $U+V$ and DFT-GGA methods, respectively. Experimental [24, 51] and our theoretical phase boundaries between CDW and SC states are shown on the upper abscissa and denoted by background color changes in (b) and (c), respectively.

optical branches obtained with V also agree with experiments. Specifically, our result well matches the anomalous dispersion of LO mode along ΓX [56, 58, 59] related with the instability toward the charge ordering [58, 59].

We present doping-dependent evolution of frequencies for the selected phonon modes of BKBO and BSBO in Figs. 3(b) and (c). Our calculations with the extended Hubbard interactions fruitfully reflect the measured trends of structural distortions for the both systems. In the case of BKBO shown in Fig. 3(b), the breathing mode computed using DFT-GGA becomes to be stable when $x \geq 0.15$ while it does only when $x \geq 0.4$ in the experiments [59–61] and our results with V . BKBO with $x \geq 0.4$ show SC states without structural distortions [9, 51, 56, 62] while the tilting instabilities still remain in DFT-GGA as shown in Figs. 3 (a) and (b) [34]. This is in sharp contrast to complete absence of instability in DFT+ $U+V$ results when $x \geq 0.4$. Thus, the non-local Coulomb interaction is decisive in capturing the transition between CDW and SC states of BKBO.

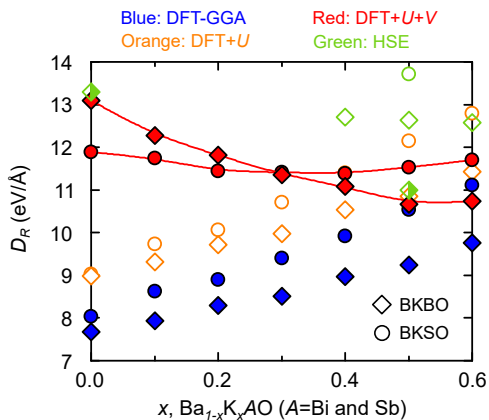


FIG. 4. Reduced e - ph matrix element (D_R^L) as a function of doping x . Diamonds (circles) denote BKB(S)O and blue, orange, and red color indicate DFT-GGA, DFT+ U , and DFT+ U + V results, respectively. Open and right-half diamonds are HSE results for the element from Ref. 35 and Ref. 33, respectively.

As already shown in Fig. 1 (b), the effect of V is not as crucial in BKSO as it is in BKBO. Nevertheless, our method makes improvements in describing experimental phase diagram as shown in Fig. 3 (c). For undoped case, DFT-GGA shows the tilting instability in addition to the breathing instability while only the latter is observed in the experiment. Our calculation with V results in a perfect fcc structure [24]. In addition, CDW phase survives up to higher doping of $x \simeq 0.4$ in DFT+ U + V calculation, which is closer to the experimental phase boundary of $x \simeq 0.5$, due to the enhanced stretching instability. Comprehensive comparisons between results from DFT+ U and DFT+ U + V and detailed discussions are in Sec. D, Figs. S2, S5 and S7 of the SM [50].

Finally, we estimate the effects of non-local interactions on e - ph coupling constant (λ) for the breathing mode that is an important factor for the SC state. Instead of calculating λ explicitly, we compute ‘reduced e - ph matrix element’ [30, 33, 63], $D_{\alpha\mathbf{q}}^{\mu\mathbf{k}} = \partial\epsilon_{\mu\mathbf{k}}/\partial\mathbf{u}_{\mathbf{q}}^{\alpha}$ to compare with previous studies based on HSE directly [33, 35]. Here, $\mathbf{u}_{\mathbf{q}}^{\alpha}$ is a displacement vector of phonon mode α with the wave-vector \mathbf{q} and $\epsilon_{\mu\mathbf{k}}$ energy of μ th band at \mathbf{k} . Specifically, following previous works [33, 35], we obtain the reduced element of D_R^L for the energy band crossing the E_F at \mathbf{k} of L point by the breathing mode at \mathbf{q} of R point (see Fig. S3 in SM [50]).

For both systems, D_R^L increases with doping within DFT-GGA and DFT+ U as shown in Fig. 4. In sharp contrast to this, the matrix element with V decreases with increasing x for BKBO while it remains more or less the same for BKSO. So, the matrix element of the latter becomes larger than that of the former for $x > 0.3$. Considering that the coupling can be roughly estimated as $\lambda \sim (D_{\alpha\mathbf{q}}^{\mu\mathbf{k}}/\omega_{\mathbf{q}}^{\alpha})^2$ for phonon frequency $\omega_{\mathbf{q}}^{\alpha}$ [30, 33, 63],

Fig. 4 implies a higher T_c of BKSO than BKBO at larger doping levels with V , agreeing with a recent experiment [24]. We also note that our estimations are consistent with two previous HSE results for a few selected dopings [33, 35].

The opposite trends of D_R^L ’s for different computational methods can be understood by considering intersite interactions under lattice distortions. The paired octahedra with the breathing modes in Fig. 1 have an elongated long bond (LB) and a shrinking short bond (SB) between Bi(Sb) and oxygens [24]. Based on a perturbation theory, D_R^L can be written as $D_R^L\delta u_B \simeq \epsilon_{\text{SB}} - \epsilon_{\text{LB}} - V(n_{\text{SB}} - n_{\text{LB}})$ where $\epsilon_{\text{SB(LB)}}$ and $n_{\text{SB(LB)}}$ are energy level and density matrix for SB(LB), respectively, and δu_B is the perturbation amplitude of the breathing mode (See SM [50] for detailed derivations). Since $n_{\text{LB}} > n_{\text{SB}}$ for lower dopings, the intersite interaction should enhance the matrix elements over those from DFT-GGA and DFT+ U . As doping level is increased, the difference between n_{LB} and n_{SB} diminishes so that the effect of nonlocal interactions vanishes as shown in Fig. 4, thus highlighting again a critical role of V for doping dependent electron-phonon interactions.

In summary, we present a comprehensive study on the doping dependent electronic and structural properties of prototypical charge ordered materials, BKBO and BKSO using a newly developed *ab initio* computational method. We demonstrated that the non-local Coulomb interactions between the nearest neighbours are essential physical parameters in determining the doping dependent evolution of CDW and SC states, highlighting nontrivial relationships between the nonlocal interaction, charge order and lattice distortion in correlated materials.

B.G.J. M. K. and W. I. were supported by KIAS individual Grants (No. QP081301, CG083501, QP090101). S.-H.J. was supported by NRF of Korea (Grant No. 2022R1A2C1006530) funded by the Korea government (MSIT). Y.-W.S. was supported by NRF of Korea (Grant No. 2017R1A5A1014862, SRC program: vdWMRC center) and KIAS individual Grant (No. CG031509). Computations were supported by the CAC of KIAS.

* Present Address: Theoretical Division, Los Alamos National Laboratory, Los Alamos, New Mexico 87545, USA

† Email: garix.minjae.kim@gmail.com

‡ Email: hand@kias.re.kr

- [1] E. Verwey, Electronic conduction of magnetite (Fe_3O_4) and its transition point at low temperatures, *Nature* **144**, 327 (1939).
- [2] Y. Yamada, O. Hino, S. Nohdo, R. Kanao, T. Inami, and S. Katano, Polaron Ordering in Low-Doping $\text{La}_{1-x}\text{Sr}_x\text{MnO}_3$, *Phys. Rev. Lett.* **77**, 904 (1996).
- [3] B. B. Van Aken, O. D. Jurchescu, A. Meetsma, Y. Tomioka, Y. Tokura, and T. T. M. Palstra, Orbital-order-induced metal-insulator transition in

- $\text{La}_{1-x}\text{Ca}_x\text{MnO}_3$, *Phys. Rev. Lett.* **90**, 066403 (2003).
- [4] J. Tranquada, B. Sternlieb, J. Axe, Y. Nakamura, and S. Uchida, Evidence for stripe correlations of spins and holes in copper oxide superconductors, *Nature* **375**, 561 (1995).
- [5] E. H. da Silva Neto, P. Aynajian, A. Frano, R. Comin, E. Schierle, E. Weschke, A. Gyenis, J. Wen, J. Schneeloch, Z. Xu, S. Ono, G. Gu, M. L. Tacon, and A. Yazdani, Ubiquitous interplay between charge ordering and high-temperature superconductivity in cuprates, *Science* **343**, 393 (2014).
- [6] E. H. da Silva Neto, R. Comin, F. He, R. Sutarto, Y. Jiang, R. L. Greene, G. A. Sawatzky, and A. Damascelli, Charge ordering in the electron-doped superconductor $\text{Nd}_{2-x}\text{Ce}_x\text{CuO}_4$, *Science* **347**, 282 (2015).
- [7] A. Frano, S. Blanco-Canosa, B. Keimer, and R. J. Birgeneau, Charge ordering in superconducting copper oxides, *J. Phys.: Condens. Matter.* **32**, 374005 (2020).
- [8] L. Mattheiss, E. Gyorgy, and D. Johnson Jr, Superconductivity above 20 K in the Ba-K-Bi-O system, *Phys. Rev. B* **37**, 3745 (1988).
- [9] R. J. Cava, B. Batlogg, J. J. Krajewski, R. Farrow, L. W. Rupp, A. E. White, K. Short, W. F. Peck, and T. Kometani, Superconductivity near 30 K without copper: the $\text{Ba}_{0.6}\text{K}_{0.4}\text{BiO}_3$ perovskite, *Nature* **332**, 814 (1988).
- [10] A. Ramirez, Colossal magnetoresistance, *J. Phys.: Condens. Matter.* **9**, 8171 (1997).
- [11] J. Van Den Brink and D. I. Khomskii, Multiferroicity due to charge ordering, *J. Phys.: Condens. Matter.* **20**, 434217 (2008).
- [12] J. P. Attfield, Charge ordering in transition metal oxides, *Sol. State Sci.* **8**, 861 (2006).
- [13] W. Kohn and L. J. Sham, Self-consistent equations including exchange and correlation effects, *Phys. Rev.* **140**, A1133 (1965).
- [14] J. P. Perdew, J. A. Chevary, S. H. Vosko, K. A. Jackson, M. R. Pederson, D. J. Singh, and C. Fiolhais, Atoms, molecules, solids, and surfaces: Applications of the generalized gradient approximation for exchange and correlation, *Phys. Rev. B* **46**, 6671 (1992).
- [15] V. Anisimov, I. Elfimov, N. Hamada, and K. Terakura, Charge-ordered insulating state of Fe_3O_4 from first-principles electronic structure calculations, *Phys. Rev. B* **54**, 4387 (1996).
- [16] T. Tsumuraya, H. Seo, and T. Miyazaki, First-principles study of the charge ordered phase in $\kappa - \text{D}_3(\text{Cat-EDT-TTF/ST})_2$: Stability of π -electron deuterium coupled ordering in hydrogen-bonded molecular conductors, *Phys. Rev. B* **101**, 045114 (2020).
- [17] J. Hubbard, Electron correlations in narrow energy bands, *Proc. Roy. Soc. A* **276**, 238 (1963).
- [18] M. Schüler, M. Rösner, T. Wehling, A. Lichtenstein, and M. Katsnelson, Optimal Hubbard models for materials with nonlocal coulomb interactions: graphene, silicene, and benzene, *Phys. Rev. Lett.* **111**, 036601 (2013).
- [19] H. Seo, Charge ordering in organic ET compounds, *J. Phys. Soc. Jpn.* **69**, 805 (2000).
- [20] S. Yamamoto, T. Fujiwara, and Y. Hatsugai, Electronic structure of charge and spin stripe order in $\text{La}_{2-x}\text{Sr}_x\text{NiO}_4$ ($x = \frac{1}{3}, \frac{1}{2}$), *Phys. Rev. B* **76**, 165114 (2007).
- [21] H. Terletska, T. Chen, and E. Gull, Charge ordering and correlation effects in the extended Hubbard model, *Phys. Rev. B* **95**, 115149 (2017).
- [22] D. Cox and A. Sleight, Crystal structure of $\text{Ba}_2\text{Bi}^{3+}\text{Bi}^{5+}\text{O}_6$, *Solid State Commun.* **19**, 969 (1976).
- [23] D. E. Cox and A. W. Sleight, Mixed-Valent $\text{Ba}_2\text{Bi}^{3+}\text{Bi}^{5+}\text{O}_6$: Structure and Properties, *Acta. Cryst.* **B35**, 1 (1979).
- [24] M. Kim, G. M. McNally, H.-H. Kim, M. Oudah, A. S. Gibbs, P. Manuel, R. J. Green, R. Sutarto, T. Takayama, A. Yaresko, U. Wedig, M. Isobe, R. K. Kremer, D. A. Bonn, B. Keimer, and H. Takagi, Superconductivity in $(\text{Ba},\text{K})\text{SbO}_3$, *Nature Materials* **10.1038/s41563-022-01203-7** (2022).
- [25] A. I. Liechtenstein, I. I. Mazin, C. O. Rodriguez, O. Jepsen, O. K. Andersen, and M. Methfessel, Structural phase diagram and electron-phonon interaction in $\text{Ba}_{1-x}\text{K}_x\text{BiO}_3$, *Phys. Rev. B* **44**, 5388 (1991).
- [26] V. Meregalli and S. Y. Savrasov, Electron-phonon coupling and properties of doped BaBiO_3 , *Phys. Rev. B* **57**, 14453 (1998).
- [27] V. Meregalli and S. Y. Savrasov, Electron-phonon coupling and properties of doped BaBiO_3 , *J. Supercond. Nov. Magn.* **12**, 185 (1999).
- [28] T. Thonhauser and K. M. Rabe, Fcc breathing instability in BaBiO_3 from first principles, *Phys. Rev. B* **73**, 212106 (2006).
- [29] D. Korotin, V. Kukolev, A. V. Kozhevnikov, D. Novoselov, and V. I. Anisimov, Electronic correlations and crystal structure distortions in BaBiO_3 , *J. Phys.: Condens. Matter* **24**, 415603 (2012).
- [30] D. M. Korotin, D. Novoselov, and V. I. Anisimov, Correlation effects and phonon modes softening with doping in $\text{Ba}_{1-x}\text{K}_x\text{BiO}_3$, *J. Phys.: Condens. Matter.* **26**, 195602 (2014).
- [31] C. Franchini, A. Sanna, M. Marsman, and G. Kresse, Structural, vibrational, and quasiparticle properties of the Peierls semiconductor BaBiO_3 : A hybrid functional and self-consistent GW +vertex-corrections study, *Phys. Rev. B* **81**, 1 (2010).
- [32] C. Franchini, G. Kresse, and R. Podloucky, Polaronic hole trapping in doped BaBiO_3 , *Phys. Rev. Lett.* **102**, 256402 (2009).
- [33] Z. P. Yin, A. Kutepov, and G. Kotliar, Correlation-enhanced electron-phonon coupling: Applications of GW and screened hybrid functional to bismuthates, chloronitrides, and other high- T_c superconductors, *Phys. Rev. X* **3**, 021011 (2013).
- [34] Z. Li, G. Antonius, M. Wu, F. H. Da Jornada, and S. G. Louie, Electron-Phonon Coupling from Ab Initio Linear-Response Theory within the GW Method: Correlation-Enhanced Interactions and Superconductivity in $\text{Ba}_{1-x}\text{K}_x\text{BiO}_3$, *Phys. Rev. Lett.* **122**, 186402 (2019).
- [35] Z. Yuan, P. Zheng, Y. Peng, R. Liu, X. Ma, G. Wang, T. Yu, and Z. Yin, Correlation-enhanced electron-phonon coupling and superconductivity in $(\text{Ba}, \text{K})\text{SbO}_3$ superconductors, *Phys. Rev. B* **105**, 014517 (2022).
- [36] L. A. Agapito, S. Curtarolo, and M. Buongiorno Nardelli, Reformulation of $\text{DFT} + U$ as a Pseudohybrid Hubbard Density Functional for Accelerated Materials Discovery, *Phys. Rev. X* **5**, 011006 (2015).
- [37] N. Tancogne-Dejean, M. A. Sentef, and A. Rubio, Ultrafast Modification of Hubbard U in a Strongly Correlated Material: Ab initio High-Harmonic Generation in NiO , *Phys. Rev. Lett.* **121**, 097402 (2018).

- [38] S.-H. Lee and Y.-W. Son, First-principles approach with a pseudohybrid density functional for extended hubbard interactions, *Phys. Rev. Research* **2**, 043410 (2020).
- [39] N. Tancogne-Dejean and A. Rubio, Parameter-free hybridlike functional based on an extended Hubbard model: DFT + $U + V$, *Phys. Rev. B* **102**, 155117 (2020).
- [40] V. L. Campo Jr and M. Cococcioni, Extended DFT+ $U + V$ method with on-site and inter-site electronic interactions, *J. Phys.: Condens. Matter* **22**, 055602 (2010).
- [41] J. Huang, S.-H. Lee, Y.-W. Son, A. Supka, and S. Liu, First-principles study of two-dimensional ferroelectrics using self-consistent Hubbard parameters, *Phys. Rev. B* **102**, 165157 (2020).
- [42] H. J. Kulik and N. Marzari, Transition-metal dioxides: A case for the intersite term in hubbard-model functionals, *J. Chem. Phys.* **134**, 094103 (2011).
- [43] M. Cococcioni and N. Marzari, Energetics and cathode voltages of LiMPO₄ olivines ($M = \text{Fe, Mn}$) from extended Hubbard functionals, *Phys. Rev. Materials* **3**, 033801 (2019).
- [44] C. Ricca, I. Timrov, M. Cococcioni, N. Marzari, and U. Aschauer, Self-consistent DFT + $U + V$ study of oxygen vacancies in SrTiO₃, *Phys. Rev. Research* **2**, 023313 (2020).
- [45] I. Timrov, F. Aquilante, L. Binci, M. Cococcioni, and N. Marzari, Pulay forces in density-functional theory with extended Hubbard functionals: From nonorthogonalized to orthogonalized manifolds, *Phys. Rev. B* **102**, 235159 (2020).
- [46] W. Yang, S.-H. Jhi, S.-H. Lee, and Y.-W. Son, Ab initio study of lattice dynamics of group IV semiconductors using pseudohybrid functionals for extended Hubbard interactions, *Phys. Rev. B* **104**, 104313 (2021).
- [47] I. Timrov, N. Marzari, and M. Cococcioni, Self-consistent hubbard parameters from density-functional perturbation theory in the ultrasoft and projector-augmented wave formulations, *Phys. Rev. B* **103**, 045141 (2021).
- [48] I. Timrov, F. Aquilante, M. Cococcioni, and N. Marzari, Accurate electronic properties and intercalation voltages of olivine-type Li-ion cathode materials from extended hubbard functionals, *PRX Energy* **1**, 033003 (2022).
- [49] W. Yang, B. G. Jang, Y.-W. Son, and S.-H. Jhi, Lattice dynamical properties of antiferromagnetic oxides calculated using self-consistent extended hubbard functional method, *J. of Phys.: Condens. Matter* **34**, 295601 (2022).
- [50] Supplementary Materials for detailed computational methods, comprehensive phonon dispersions and self-consistent extended Hubbard parameters, which includes Ref. [64–68].
- [51] S. Pei, J. D. Jorgensen, B. Dabrowski, D. G. Hinks, D. R. Richards, A. W. Mitchell, J. M. Newsam, S. K. Sinha, D. Vaknin, and A. J. Jacobson, Structural phase diagram of the Ba_{1-x}K_xBiO₃, *Phys. Rev. B* **41**, 4126 (1990).
- [52] B. J. Kennedy, C. J. Howard, K. S. Knight, Z. Zhang, and Q. Zhou, Structures and phase transitions in the ordered double perovskites Ba₂Bi^{III}Bi^VO₆ and Ba₂Bi^{III}Sb^VO₆, *Acta Cryst. B* **62**, 537 (2006).
- [53] N. C. Plumb, D. J. Gawryluk, Y. Wang, Z. Ristić, J. Park, B. Q. Lv, Z. Wang, C. E. Matt, N. Xu, T. Shang, K. Conder, J. Mesot, S. Johnston, M. Shi, and M. Radović, Momentum-Resolved Electronic Structure of the High-Tc Superconductor Parent Compound BaBiO₃, *Phys. Rev. Lett.* **117**, 1 (2016), 1603.01745.
- [54] J. S. Oh, M. Kim, G. Kim, H. G. Lee, H. K. Yoo, S. Sinn, Y. J. Chang, M. Han, C. Jozwiak, A. Bostwick, E. Rotenberg, H. D. Kim, and T. W. Noh, Evidence for absence of metallic surface states in BiO₂-terminated BaBiO₃ thin films, *Curr. Appl. Phys.* **18**, 658 (2018).
- [55] A. Togo and I. Tanaka, First principles phonon calculations in materials science, *Scr. Mater.* **108**, 1 (2015).
- [56] M. Braden, W. Reichardt, W. Schmidbauer, A. S. Ivanov, and A. Y. Rumiantsev, Lattice dynamics of (Ba/K)BiO₃, *J. Supercond.* **8**, 595 (1995).
- [57] C. K. Loong, P. Vashishta, R. K. Kalia, W. Jin, M. H. Degani, D. G. Hinks, D. L. Price, J. D. Jorgensen, B. Dabrowski, A. W. Mitchell, D. R. Richards, and Y. Zheng, Phonon density of states and oxygen-isotope effect in Ba_{1-x}K_xBiO₃, *Phys. Rev. B* **45**, 8052 (1992).
- [58] M. Braden, W. Reichardt, A. S. Ivanov, and A. Y. Rumiantsev, Anomalous dispersion of LO phonon branches in Ba_{0.6}K_{0.4}BiO₃, *Europhys. Lett.* **34**, 531 (1996).
- [59] M. Braden, W. Reichardt, S. Shiryayev, and S. N. Barilo, Giant phonon anomalies in the bond-stretching modes in doped BaBiO₃: Comparison to cuprates manganites and nickelates, *Phys. C Supercond. its Appl.* **378-381**, 89 (2002).
- [60] S. Tajima, M. Yoshida, N. Koshizuka, H. Sato, and S. Uchida, Raman-scattering study of the metal-insulator transition in Ba_{1-x}K_xBiO₃, *Phys. Rev. B* **46**, 1232 (1992).
- [61] M. Braden, W. Reichardt, E. Elkaim, J. P. Lauriat, S. Shiryayev, and S. N. Barilo, Structural distortion in superconducting Ba_{1-x}K_xBiO₃, *Phys. Rev. B* **62**, 6708 (2000).
- [62] R. M. Fleming, P. Marsh, R. J. Cava, and J. J. Krajewski, Temperature dependence of the lattice parameters in the 30-K superconductor Ba_{0.6}K_{0.4}BiO₃, *Phys. Rev. B* **38**, 7026 (1988).
- [63] C.-J. Kang and G. Kotliar, Material design of indium-based compounds: Possible candidates for charge, valence, and bond disproportionation and superconductivity, *Phys. Rev. Materials* **3**, 015001 (2019).
- [64] N. J. Mosey and E. A. Carter, Ab initio evaluation of coulomb and exchange parameters for DFT + U calculations, *Phys. Rev. B* **76**, 155123 (2007).
- [65] N. J. Mosey, P. Liao, and E. A. Carter, Rotationally invariant ab initio evaluation of coulomb and exchange parameters for dft+ u calculations, *J. Chem. Phys.* **129**, 014103 (2008).
- [66] P. Giannozzi, S. Baroni, N. Bonini, M. Calandra, R. Car, C. Cavazzoni, D. Ceresoli, G. L. Chiarotti, M. Cococcioni, I. Dabo, *et al.*, QUANTUM ESPRESSO: a modular and open-source software project for quantum simulations of materials, *J. Phys.: Condens. Matter* **21**, 395502 (2009).
- [67] M. J. van Setten, M. Giantomassi, E. Bousquet, M. J. Verstraete, D. R. Hamann, X. Gonze, and G.-M. Rignanese, The PseudoDojo: Training and grading a 85 element optimized norm-conserving pseudopotential table, *Comp. Phys. Comm.* **226**, 39 (2018).
- [68] G. Kim, M. Neumann, M. Kim, M. D. Le, T. D. Kang, and T. W. Noh, Suppression of Three-Dimensional Charge Density Wave Ordering via Thickness Control, *Phys. Rev. Lett.* **115**, 1 (2015).

SUPPLEMENTARY INFORMATION

A. Pseudohybrid density functional for extended Hubbard interactions

The total energy formula with the extended Hubbard interactions including both on-site and intersite Coulomb interaction (U and V) is given by [40]

$$E_{\text{DFT}+U+V} = E_{\text{DFT}} + E_{\text{UV}}, \quad (\text{S1})$$

where E_{DFT} is the (semi)local density functional and E_{UV} the extended Hubbard functional. Within a rotationally invariant form with the fully localized limit (FLL) double counting correction, E_{UV} is written as [40]

$$E_{\text{UV}} = \sum_I \sum_{mm'\sigma} \frac{U^I}{2} (\delta_{mm'} - n_{mm'}^{II\sigma}) n_{m'\sigma}^{II\sigma} - \sum_{\{I,J\}} \sum_{mm'\sigma} \frac{V^{IJ}}{2} n_{mm'}^{IJ\sigma} n_{m'\sigma}^{JI\sigma}, \quad (\text{S2})$$

where the generalized occupation matrix is $n_{mm'}^{IJ\sigma} = \sum_{\mathbf{k}\nu} f_{\mathbf{k}\nu}^\sigma \langle \psi_{\mathbf{k}\nu}^\sigma | \phi_{m'}^J \rangle \langle \phi_m^I | \psi_{\mathbf{k}\nu}^\sigma \rangle$, $f_{\mathbf{k}\nu}^\sigma$ the Fermi-Dirac function of Kohn-Sham orbital of $\psi_{\mathbf{k}\nu}^\sigma$ of the ν th band with spin σ at momentum \mathbf{k} . The Löwdin orthonormalized atomic wave function, ϕ_m^I is used as a projector for the localized atomic orbital where m is angular quantum number. Here, I and J are abbreviated indexes for atomic positions and principal and azimuthal quantum numbers together. $\{I, J\}$ in Eq. S2 denotes a pair of atoms within the nearest neighboring distances.

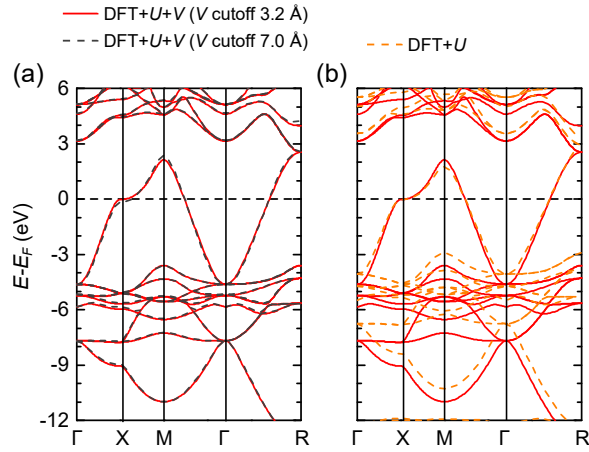


FIG. S1. (a) Energy bands of BBO of cubic perovskite structure obtained from DFT+U+V with different V cutoff length. For 3.2 Å cutoff case, only the nearest Bi-O pairs are considered while up to 3rd nearest Bi-O pairs are considered for 7.0 Å cutoff case. (b) Comparison between energy band obtained from DFT+U (U_s^{Bi} , U_p^{Bi} , and U_p^O) and DFT+U+V. Here, U_o^A for o -orbital of atom A shown in Table S2

TABLE S1. Calculated structural and electronic properties of BBO along with computational and experimental data from previous studies. v : volume, β : monoclinic angle, δ_B : breathing distortion, θ_T : tilting distortion, and E_g : band gap

	DFT-GGA	DFT+U (w/o O 2p)	DFT+U	DFT+U+V
v (Å ³)	85.03	85.03	82.19	82.94
β (deg)	90.39	90.40	90.27	90.34
δ_B (Å)	0.08	0.08	0.10	0.10
θ_T (°)	11.75	11.76	9.71	10.46
E_g (eV)	0.00	0.00	0.71	0.99
U_p^{Bi}	-	0.14	0.09	0.11
U_p^O	-	-	8.38	8.23

B. Calculation details

Following the ansatz by Mosey *et al.* [64, 65], we extend the ACBN0 pseudohybrid functional for U [36] into V [38] by considering the renormalized occupation number $N_{\psi_{\mathbf{k}\nu}}^{IJ\sigma}$ and density matrix $P_{mm'}^{IJ\sigma}$ for a pair of different atoms I and J :

$$N_{\psi_{\mathbf{k}\nu}}^{IJ\sigma} = \sum_I \sum_m \langle \psi_{\mathbf{k}\nu}^\sigma | \phi_m^I \rangle \langle \phi_m^I | \psi_{\mathbf{k}\nu}^\sigma \rangle + \sum_J \sum_{m'} \langle \psi_{\mathbf{k}\nu}^\sigma | \phi_{m'}^J \rangle \langle \phi_{m'}^J | \psi_{\mathbf{k}\nu}^\sigma \rangle, \quad (\text{S3})$$

$$P_{mm'}^{IJ\sigma} = \sum_{\mathbf{k}\nu} w_{\mathbf{k}} f_{\mathbf{k}\nu} N_{\psi_{\mathbf{k}\nu}}^{IJ\sigma} \langle \psi_{\mathbf{k}\nu}^\sigma | \phi_m^I \rangle \langle \phi_{m'}^J | \psi_{\mathbf{k}\nu}^\sigma \rangle, \quad (\text{S4})$$

where $w_{\mathbf{k}}$ is \mathbf{k} -point weight and $f_{\mathbf{k}\nu}$ is the Fermi-Dirac function of the Bloch state $|\psi_{\mathbf{k}\nu}^\sigma\rangle$. By using Eq. S3 and S4, U^I , J^I , and V^{IJ} can be defined as [36, 38, 39]:

$$U^I = \frac{\sum_{m, \dots, m'''} \sum_{\sigma\sigma'} P_{mm'}^{II\sigma} P_{m''m'''}^{II\sigma'} (mm'|m''m''')}{\sum_{m \neq m'} \sum_{\sigma} n_{mm}^{II\sigma} n_{m'm'}^{II\sigma} + \sum_{\{m\}} \sum_{\sigma} n_{mm}^{II\sigma} n_{m'm'}^{II-\sigma}}, \quad (\text{S5})$$

$$J^I = \frac{\sum_{m, \dots, m'''} \sum_{\sigma} P_{mm'}^{II\sigma} P_{m''m'''}^{II\sigma} (mm'|m''m''')}{\sum_{m \neq m'} \sum_{\sigma} n_{mm}^{II\sigma} n_{m'm'}^{II\sigma}}, \quad (\text{S6})$$

$$V^{IJ} = \frac{1}{2} \frac{\sum_{m, \dots, m'''} \sum_{\sigma\sigma'} [P_{mm'}^{II\sigma} P_{m''m'''}^{JJ\sigma'} - \delta_{\sigma\sigma'} P_{mm'}^{IJ\sigma} P_{m''m'''}^{JI\sigma'}] (mm'|m''m''')}{\sum_{\{m\}} \sum_{\sigma\sigma'} [n_{mm}^{II\sigma} n_{m'm'}^{JJ\sigma'} - \delta_{\sigma\sigma'} n_{mm}^{II\sigma} n_{m'm'}^{JI\sigma'}]}, \quad (\text{S7})$$

where $(mm'|m''m''') \equiv \int d\mathbf{r}_1 d\mathbf{r}_2 \phi_m^I(\mathbf{r}_1) \phi_{m'}^I(\mathbf{r}_1) |\mathbf{r}_1 - \mathbf{r}_2|^{-1} \phi_{m''}^{J*}(\mathbf{r}_2) \phi_{m'''}^J(\mathbf{r}_2)$.

We implemented the pseudohybrid density functionals for extended Hubbard interactions shown in Eqs. S5, S6, and S7 in QUANTUM ESPRESSO package [38, 46, 66]. We used the norm-conserving pseudopotentials provided by the PseudoDojo project [67]. The energy cutoff for charge density was set to 480 Ry. A $15 \times 15 \times 15$ k -point mesh was used for self-consistent calculation of perfect perovskite structure (5 atoms in the unitcell). The k -mesh density was kept the same for all other calculations. The Hubbard U and V parameters are obtained during the self-consistent calculation from Eqs. S5, S6 and S7 as shown in Table S2.

The potassium (K) substitution effects are simulated by reducing the number of electrons in the unitcell and

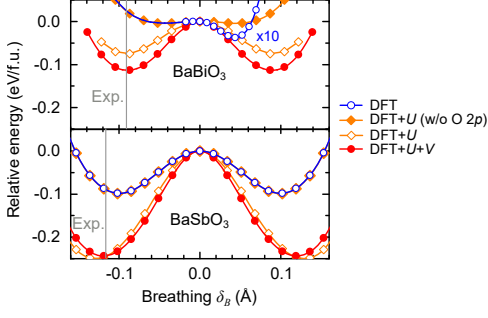


FIG. S2. Double well potential as a function of δ_B . Blue, orange closed diamond, orange open diamond, and red indicate DFT-GGA, DFT+ U (U_s^{Bi} , U_p^{Bi}), DFT+ U (U_s^{Bi} , U_p^{Bi}), and U_p^O), and DFT+ $U+V$ respectively.

inserting a compensating background charge. For lattice optimization with doping, we used large cubic supercell structures containing 40 atoms to model realistic doping. As shown in Fig. S3, our optimized pseudocubic lattice parameter of a_P using DFT+ $U+V$ formalism agrees with experimental data [24, 51] very well while DFT-GGA fails. With these optimized structures, the phonon dispersions were calculated using the finite displacement method by Phonopy [55]. We used fixed U and V values, which are obtained from the equilibrium structure, to calculate the supercell structures with atomic displacement. Full phonon band structures of BKBO and BKSO are shown in Fig. S4.

For the direct comparison with the previous HSE result (Fig.4 of main text), the reduced matrix element for estimating e - ph interaction is obtained by using the same scheme used in Ref. 33. For example, the breathing distortion induces band splitting as shown Fig. S6. The energy splitting at L point (ΔE) is used to determine the matrix element with the given oxygen displacement.

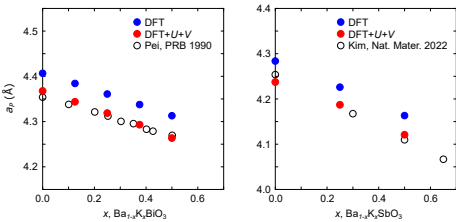


FIG. S3. Experimental pseudocubic lattice parameter a_P as a function of K doping of x for BKBO and BKSO [24, 51]. Cubic supercell structures up to 40 atoms are used to model realistic K substitution structures. DFT-GGA calculations overestimate the lattice constant while DFT+ $U+V$ results well agree with experimental observations.

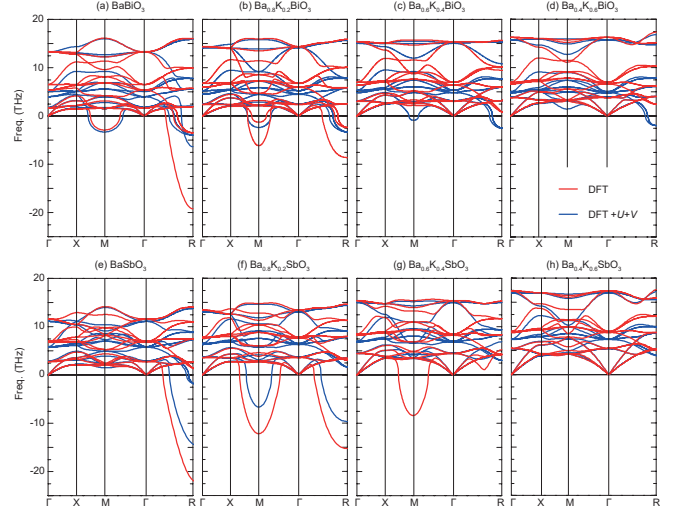


FIG. S4. Phonon band structures of BKBO and BKSO. Blue and red lines indicate DFT and DFT+ $U+V$ results, respectively.

C. Doping dependence of the reduced el - ph matrix elements

The essential trend of the K doping (x) dependent variation of the reduced el - ph matrix (D_R^L) of $Ba_{1-x}K_xAO_3$ ($A=Bi, Sb$) shown in Fig. 4 of the main text can be understood by considering simplified perturbative expansions of interactions within DFT+ $U+V$ scheme. The extended Hubbard interactions are treated as perturbations to the Kohn-Sham (KS) equation of (semi)local functional such that

$$\mathcal{H}_{\text{total}} = \mathcal{H}_{\text{DFT}} + \mathcal{H}_{UV} \quad (\text{S8})$$

TABLE S2. Calculated U and V (in eV) for $BaA_{1-x}K_xO_3$ ($A = Bi$ and Sb). $U_{s(p)}^A$ (U_p^O) is on-site Hubbard parameters of valence $s(p)$ orbital of $A(O)$ atom. $V_{sp(pp)}$ is the inter-site Hubbard parameters between $s(p)$ orbital of A and p orbital of O . V_{sp}^{Ba} is the inter-site Hubbard parameters of between s orbital of Ba and p orbital of O .

x	U_s^{Bi}	U_p^{Bi}	U_p^O	V_{sp}	V_{pp}	V_{sp}^{Ba}	U_s^{Sb}	U_p^{Sb}	U_p^O	V_{sp}	V_{pp}	V_{sp}^{Ba}
0.00	1.03	0.11	8.18	1.78	1.59	0.77	0.92	0.13	8.18	1.86	1.61	0.75
0.05	1.00	0.11	8.17	1.76	1.58	0.76	0.95	0.13	8.15	1.82	1.59	0.74
0.10	0.98	0.11	8.15	1.74	1.58	0.75	0.91	0.13	8.12	1.78	1.58	0.74
0.15	0.96	0.11	8.14	1.72	1.57	0.75	0.88	0.13	8.08	1.74	1.56	0.73
0.20	0.94	0.11	8.13	1.70	1.56	0.74	0.85	0.13	8.05	1.71	1.55	0.72
0.25	0.92	0.11	8.11	1.68	1.56	0.74	0.83	0.12	8.01	1.68	1.54	0.71
0.30	0.90	0.11	8.09	1.66	1.55	0.73	0.80	0.12	7.97	1.65	1.52	0.71
0.35	0.89	0.11	8.08	1.64	1.54	0.72	0.78	0.12	7.93	1.63	1.51	0.69
0.40	0.87	0.11	8.06	1.63	1.54	0.72	0.76	0.12	7.89	1.60	1.49	0.68
0.45	0.85	0.10	8.04	1.61	1.52	0.72	0.74	0.12	7.84	1.58	1.48	0.68
0.50	0.83	0.10	8.02	1.59	1.52	0.70	0.72	0.12	7.79	1.55	1.46	0.67
0.55	0.81	0.10	8.00	1.57	1.51	0.70	0.70	0.12	7.74	1.53	1.44	0.66
0.60	0.80	0.10	7.98	1.56	1.50	0.69	0.68	0.12	7.69	1.51	1.43	0.65

where $\mathcal{H}_{\text{total}}\psi_{\mathbf{k}\nu}^{\sigma} = \epsilon_{\mathbf{k}\nu}^{\sigma}\psi_{\mathbf{k}\nu}^{\sigma}$ and $\mathcal{H}_{\text{DFT}}\varphi_{\mathbf{k}\nu}^{\sigma} \equiv [-\nabla^2 + V_{\text{DFT}}]\varphi_{\mathbf{k}\nu}^{\sigma} = \epsilon_{\mathbf{k}\nu}^{\sigma}\varphi_{\mathbf{k}\nu}^{\sigma}$. Here, V_{DFT} is the KS potential corresponding to (semi)local energy functional (E_{DFT}) and $\varphi_{\mathbf{k}\nu}^{\sigma}$ the KS wavefunction with eigenvalue of $\epsilon_{\mathbf{k}\nu}^{\sigma}$. The perturbation can be written as $\mathcal{H}_{\text{UV}}\psi_{\mathbf{k}\nu}^{\sigma} = \delta E_{\text{UV}}/\delta(\psi_{\mathbf{k}\nu}^{\sigma})^*$. As discussed above, we only consider the alternation of energy bands crossing the Fermi level at the L point in the presence of breathing distortion at the R point as shown in Fig S6 so that the momentum, spin and band indexes will be dropped hereafter.

The energy band considered here mainly originate from the anti-bonding state between s orbital of Bi (Sb) at the center of octahedra and p orbitals of oxygen at their vertices [68]. Thus, the pair of distorted perovskites (see Fig. 1a of the main text) has elongated and shortened bonds for the anti-bonding states. We will call them the long and short bonding (LB and SB), respectively. From these considerations, the split energies of the band by the breathing mode in Fig. S6 can be approximated as energy eigenvalues of ϵ_{LB} and ϵ_{SB} (or ε_{LB} and ε_{SB} without \mathcal{H}_{UV}) for the static atomic configurations associated with LB and SB, respectively. The resulting difference of $\epsilon_{\text{SB}} - \epsilon_{\text{LB}}$ (or $\varepsilon_{\text{SB}} - \varepsilon_{\text{LB}}$ without \mathcal{H}_{UV}) can be assigned as D_R^L because the energy level of the anti-bonding SB is higher than that of the LB.

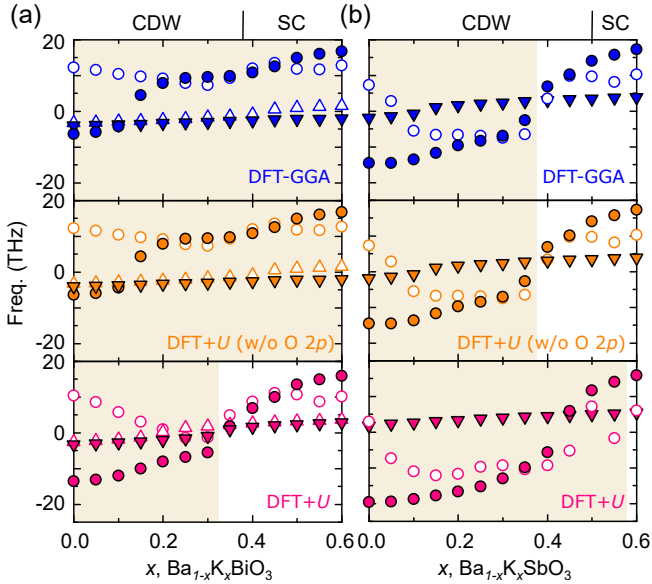


FIG. S5. Phonon frequency variations of the four modes as increasing K doping level in (a) BKBO and (b) BKSO. Top, middle, and bottom panels are for the modes obtained by DFT-GGA, DFT+U (U_s^{Bi}, U_p^{Bi}), and DFT+U (U_s^{Bi}, U_p^{Bi} , and U_p^O) methods, respectively. Experimental [24, 51] and our theoretical phase boundaries between CDW and SC states are shown on the upper abscissa and denoted by background color changes in (a) and (b), respectively.

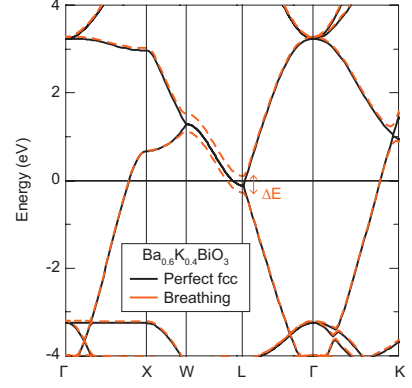


FIG. S6. Electronic band structure of $\text{Ba}_{0.6}\text{K}_{0.4}\text{BiO}_3$ with and without the oxygen-breathing displacement obtained from DFT+U+V. The breathing distortion induces band splitting depicted by orange dotted lines. The band splitting of ΔE indicated by the arrow are used to calculate the reduced e - ph matrix element of D_R^L .

With the amplitude δu_B of the breathing mode, the E_{DFT} contribution is simply written as $D_R^L \cdot \delta u_B = \varepsilon_{\text{SB}} - \varepsilon_{\text{LB}}$. In case of a pristine octahedron, we can assign an overlap integral (t_{sp}) between p orbital of oxygen and s orbital of Bi(Sb) and the orbital energies for as ω_p and ω_s respectively. Then, with distorted structures by the breathing mode, the energy splitting can be expressed up to the second order of t_{sp} as follows,

$$D_R^L \delta u_B = \varepsilon_{\text{SB}} - \varepsilon_{\text{LB}} \sim \frac{4t_{sp}^2 \delta \tau_{sp}}{|\omega_p - \omega_s|}, \quad (\text{S9})$$

where t_{sp} changes to $t_{sp}(1 \pm \delta \tau_{sp})$ for SB (LB) and $|\omega_p - \omega_s| \gg t_{sp}$ is assumed. We note that the K doping (x) enhances the hole contribution to the p orbital, thereby reducing the $|\omega_p - \omega_s|$. So, Eq. S9 implies that D_R^L based on DFT-GGA increases with x , explaining the increasing matrix elements shown in Fig. 4. We also note that a small contraction of lattice constant with doping in Fig. S3 also could increase t_{sp} , thus corroborating the trend.

With onsite and intersite Hubbard interaction for s orbital of Bi(Sb) and p orbital oxygen (U_p and V_{sp}), the perturbative Hamiltonian for the Hubbard interactions can be written as

$$\mathcal{H}_{\text{UV}} = \mathcal{H}_U + \mathcal{H}_V \equiv U_p(1 - 2n_{pp}) - V_{sp}n_{sp}, \quad (\text{S10})$$

where n_{pp} is the density matrix for the p orbital of oxygen and n_{sp} the generalized one for the neighboring s orbital of Bi(Sb) and oxygen p orbitals. Here, the spin index is suppressed and the significantly smaller onsite energy for s orbital as shown in Table. S2 is neglected. For $n_{pp} \neq 0$, the onsite Hubbard energy shifts the oxygen level of ω_p toward ω_s so that, according to Eq. S9, the resulting D_R^L should enhance compared with those from

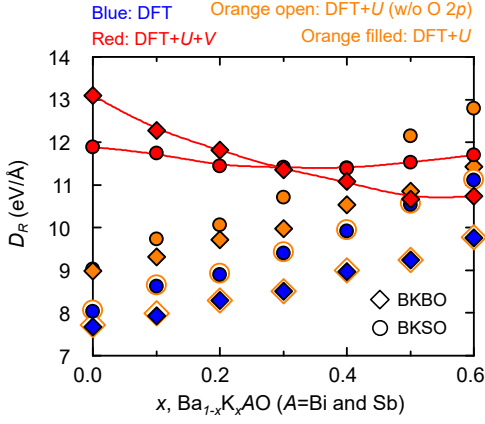


FIG. S7. Reduced e - ph matrix element (D_R^L) as a function of doping x . Diamonds (circles) denote BKB(S)O and blue, orange open, orange filled and red color indicate DFT-GGA, DFT+ U (U_s^{Bi}, U_p^{Bi}), DFT+ U (U_s^{Bi}, U_p^{Bi} , and U_p^O) and DFT+ U + V results, respectively

DFT-GGA and increases as the amount of doped potassium accumulates. This tendency is indeed confirmed by our calculation only with U as shown in Fig. 4.

From Eq. S10, we can estimate the contribution from the nonlocal interactions for the matrix element as follows,

$$D_R^L \delta u_B = \epsilon_{SB} - \epsilon_{LB} \simeq \tilde{\epsilon}_{SB} - \tilde{\epsilon}_{LB} - V_{sp}(n_{sp}^{SB} - n_{sp}^{LB}), \quad (\text{S11})$$

where $\tilde{\epsilon}_{SB(LB)}$ is the renormalized energy level of Eq. S9 by the on-site energy of U_p in Eq. S10 and $n_{sp}^{SB(LB)}$ is the generalized density matrix for the SB (LB). Here we note that we neglect the perturbation to the wave function in considering Eq. S11 that seems to be smaller than the variations of density matrix under perturbations. The density matrix for the lower energy state should be larger than that for the higher, i.e., $n_{sp}^{LB} > n_{sp}^{SB}$ so that Eq. S11 immediately implies the enhanced D_R^L with V as shown in Fig. 4 of the main text. Furthermore, as doping increases, the charge disproportionation or difference between the SB and LB should decrease and then disappear as x approaches 1. Therefore, $n_{sp}^{SB} - n_{sp}^{LB}$ in Eq. S11

decreases to zero as doping increases so that the effect of intersite Hubbard interactions to D_R^L diminishes as x increases as shown in Fig. 4.

D. Comparison between DFT+ U and DFT+ U + V

Like in the previous study [29], DFT+ U on Bi s (and p) atomic orbital does not give any improvement compared to DFT-GGA method. The optimized crystal structure (Table S1), double well potential (Fig. S2), phonon frequency as a function of K doping level (Fig. S5), and reduced e - ph matrix element (Fig. S7) obtained from DFT+ U (U_s^{Bi}, U_p^{Bi}) [or labeled as DFT+ U (w/o O 2 p)] are consistent with those from DFT-GGA.

When U_p^O is included in DFT+ U calculation, it seemingly gives improvement for some physical properties. Unlike a typical partially filled case, the U_p^O in BB(S)O changes the energetic position of O p orbitals with respect to the Bi(Sb) s orbitals as explained in the main text. The O p level is shifted down so that the energy difference between bands for O p orbitals and the Bi(Sb) s orbital becomes smaller and the covalency between them is enhanced (Fig. 2). As a result, the breathing distortion and the band gap are enhanced compared to DFT-GGA as shown in Table S1 and Fig. S2.

However, it is still not enough to describe charge ordered phase of BB(S)O. The band gap of the monoclinic CDW phase obtained from DFT+ U (U_s^{Bi}, U_p^{Bi} , and U_p^O) is about 70% of that from DFT+ U + V and experimental observation. The computed phonon stabilities also fail to explain experimental phase boundaries as shown in Fig. S5. The most notable failure can be found in the reduced e - ph matrix element (D_R^L) as shown in Fig. S7. As already discussed in the previous section, the inclusion of U_p^O affects the energy level and the covalency so that D_R^L is enhanced compared to DFT-GGA results. However, D_R^L keeps increasing as the K doping increases like DFT-GGA result. Without intersite Coulomb interaction V , one cannot explain the e - ph coupling depending on K doping correctly as explained in the previous section. The decreasing trend of D_R^L depending K doping can be captured only in DFT+ U + V calculations and it well agrees with the previous HSE results.